UC Riverside

UC Riverside Previously Published Works

Title

Estimate of carbonyl sulfide tropical oceanic surface fluxes using Aura Tropospheric Emission Spectrometer observations

Permalink

https://escholarship.org/uc/item/7fq8s84j

Journal

Journal of Geophysical Research: Atmospheres, 120(20)

ISSN

2169-897X

Authors

Kuai, Le
Worden, John R
Campbell, J Elliott
et al.

Publication Date

2015-10-27

DOI

10.1002/2015jd023493

Peer reviewed

eScholarship.org Powered by the California Digital Library
University of California

AGU PUBLICATIONS

JGR

Journal of Geophysical Research: Atmospheres

RESEARCH ARTICLE
10.1002/2015JD023493

Key Point:
- The missing carbonyl sulfide source is found at west Pacific and Indian Ocean

Correspondence to:
L. Kuai,
kl@gps.caltech.edu

Citation:
Kuai, L., et al. (2015), Estimate of carbonyl sulfide tropical oceanic surface fluxes using Aura Tropospheric Emission Spectrometer observations, *J. Geophys. Res. Atmos.*, *120*, 11,012–11,023, doi:10.1002/2015JD023493.

Received 8 APR 2015
Accepted 28 AUG 2015
Accepted article online 4 SEP 2015
Published online 23 OCT 2015

©2015. American Geophysical Union. All Rights Reserved.

Estimate of carbonyl sulfide tropical oceanic surface fluxes using Aura Tropospheric Emission Spectrometer observations

Le Kuai[1], John R. Worden[2], J. Elliott Campbell[3], Susan S. Kulawik[4], King-Fai Li[5], Meemong Lee[2], Richard J. Weidner[2], Stephen A. Montzka[6], Fred L. Moore[6], Joe A. Berry[7], Ian Baker[8], A. Scott Denning[8], Huisheng Bian[9,10], Kevin W. Bowman[2], Junjie Liu[2], and Yuk L. Yung[11]

[1]Joint Institute for Regional Earth System Science and Engineering, University of California, Los Angles, California, USA, [2]Jet Propulsion Laboratory, California Institute of Technology, Pasadena, California, USA, [3]Sierra Nevada Research Institute, University of California, Merced, California, USA, [4]BAER Institute, NASA Ames, Mountain View, California, USA, [5]Department of Applied Mathematics, University of Washington, Seattle, Washington, USA, [6]Earth System Research Laboratory, NOAA, Boulder, Colorado, USA, [7]Department of Global Ecology, Carnegie Institution of Washington, Stanford, California, USA, [8]Department of Atmospheric Sciences, Colorado State University, Fort Collins, Colorado, USA, [9]Goddard Space Flight Center, NASA, Greenbelt, Maryland, USA, [10]JCET, University of Maryland, Baltimore, Maryland, USA, [11]Division of Geological and Planetary Sciences, California Institute of Technology, Pasadena, California, USA

Abstract Quantifying the carbonyl sulfide (OCS) land/ocean fluxes contributes to the understanding of both the sulfur and carbon cycles. The primary sources and sinks of OCS are very likely in a steady state because there is no significant observed trend or interannual variability in atmospheric OCS measurements. However, the magnitude and spatial distribution of the dominant ocean source are highly uncertain due to the lack of observations. In particular, estimates of the oceanic fluxes range from approximately 280 Gg S yr^{-1} to greater than 800 Gg S yr^{-1}, with the larger flux needed to balance a similarly sized terrestrial sink that is inferred from NOAA continental sites. Here we estimate summer tropical oceanic fluxes of OCS in 2006 using a linear flux inversion algorithm and new OCS data acquired by the Aura Tropospheric Emissions Spectrometer (TES). Modeled OCS concentrations based on these updated fluxes are consistent with HIAPER Pole-to-Pole Observations during 4th airborne campaign and improve significantly over the a priori model concentrations. The TES tropical ocean estimate of 70 ± 16 Gg S in June, when extrapolated over the whole year (about 840 ± 192 Gg S yr^{-1}), supports the hypothesis proposed by Berry et al. (2013) that the ocean flux is in the higher range of approximately 800 Gg S yr^{-1}.

1. Introduction

Carbonyl sulfide (OCS) is the most abundant sulfur-containing gas in the atmosphere. OCS plays an important role in climate-related processes of both the stratosphere and the troposphere in part because of its relatively long lifetime (2–4 years) in the troposphere [*Chin and Davis*, 1993]. For example, volcanic OCS is the primary source of stratospheric sulfate aerosol [*Chin and Davis*, 1995; *Chin and Jacob*, 1996; *Crutzen*, 1976; *Notholt et al.*, 2003, 2006; *Turco et al.*, 1980], which can alter the global radiation budget and hence the climate via the scattering of sunlight and the catalytic depletion of stratospheric ozone [*Charlson et al.*, 1990]. OCS is also a useful tracer for the carbon cycle. Unlike CO_2, which is involved in both photosynthesis and respiration, OCS is involved only in photosynthesis by plant uptake, making OCS an ideal candidate for partitioning the photosynthetic uptake from respiration and thus helping constrain gross primary production (GPP) [*Asaf et al.*, 2013; *Berry et al.*, 2013; *Campbell et al.*, 2008; *Montzka et al.*, 2007; *Wohlfahrt et al.*, 2012]. Although recent studies suggest that soil may become an OCS source at high temperature during the peak-growing season and the anthropogenic source is growing, terrestrial vegetation uptake is the predominant land flux at continental scales, supporting OCS as an independent tracer of terrestrial photosynthesis [*Campbell et al.*, 2015; *Maseyk et al.*, 2014]. Accurate knowledge of the global OCS budget will thus help better understand the global sulfur and carbon cycles.

As discussed in *Kettle et al.* [2002], and *Montzka et al.* [2007], total global, annual tropospheric OCS concentrations show little temporal variability in the last decade. Thus, the global annual source and sink should be approximately in balance. This was seemingly confirmed by the work of *Kettle et al.* [2002], who estimated a terrestrial OCS sink

of 238 Gg S yr^{-1} based on the net primary production, which is close to be balanced by their estimated oceanic source of ~280 Gg S yr^{-1} (Gg/yr of sulfate). But later modeling and observation work evaluating on the terrestrial GPP suggested that the terrestrial OCS sink may be more than doubled, ranging from 730 to 1500 Gg S yr^{-1} [*Berry et al.*, 2013; *Campbell et al.*, 2008; *Montzka et al.*, 2007; *Sandoval-Soto et al.*, 2005; *Suntharalingam et al.*, 2008], leading to the hypothesis that there is a large missing oceanic OCS source of ~600 Gg S yr^{-1} needed to close the global OCS budget [*Berry et al.*, 2013; *Launois et al.*, 2014]. However, direct measurements of the OCS ocean source term are spatially sparse, making this hypothesis difficult to evaluate. New measurements of free tropospheric OCS concentrations over ocean, as observed by the Aura Tropospheric Emissions Spectrometer (TES), are therefore valuable for providing an estimate of the OCS missing source term [*Kuai et al.*, 2014].

The TES data observed from space provide the first measurements to map the distribution of free tropospheric OCS over oceans between latitude 40°S and 40°N [*Kuai et al.*, 2014]. The sensitivity of the TES measurements to OCS distributions is weaker poleward of ±40° because the sensitivity depends on temperature. Currently, no land retrievals of OCS from TES are available because of the difficulty in disentangling variations in surface emissivity from the OCS distribution in the weak 4 μm band used to estimate OCS distributions.

In this work, we use the TES data within ±40° to perform a flux inversion with Goddard Earth Observing System-Chemistry (GEOS-Chem) as the forward model [*Suntharalingam et al.*, 2008] needed to relate observed concentrations back to surface fluxes. We then validate modeled tropospheric OCS concentrations based on updated fluxes with HIAPER Pole-to-Pole Observations (HIPPO) airborne data. Section 2 discusses the details of TES OCS data and the linear flux inversion algorithm. The proposed inversion algorithm is applied to the TES OCS observations in June 2006 because the full year of TES OCS data is not available yet. The GEOS-Chem simulated OCS concentrations using the updated fluxes from the inversion method are compared with HIPPO-4 measurements, and the new land/ocean fluxes are presented in section 3. Section 4 summarizes the findings.

2. Data and the Inversion Algorithm

2.1. TES OCS Data

Midtropospheric OCS columns have been recently retrieved from the TES infrared spectral measurements [*Kuai et al.*, 2014]. The TES nadir view data during its "Global Survey" mode were selected to map OCS over the ocean. The nadir field of view is an area of about 5 km × 8 km. The footprints of Global Surveys (operated as a "one day on, one day off" cycle) are approximately 180 km apart. On the off day, TES turns to a Special Observations mode. Those data in a Special Observations mode are not used to retrieve OCS at current stage. Each TES Global Survey takes ~26 h to complete the required 16 orbits. The Aura orbit repeats every 16 days, including 8 TES Global Surveys. Therefore, for a 1 month period, we can have about 15 Global Surveys. This sampling method ensures the monthly mean data to be averaged in a smoothing grid box (20° × 20°) with at least 50 observations. The error on the mean of such monthly mean OCS data is estimated to be about 7 parts per trillion (ppt) [*Kuai et al.*, 2014].

In this paper, we will use the TES OCS data over the ocean between the latitudes of ±40° in June 2006. Each OCS profile retrieved from a single sounding that passed quality control [*Kuai et al.*, 2014] is averaged between 900 hPa and 200 hPa to estimate the free tropospheric OCS. TES OCS data were gridded onto GEOS-Chem's spatial resolution (2° latitude × 2.5° longitude) but were smoothed by spatially averaged within 20° × 20° boxes centered at GEOS-Chem's grids. Only 1 month of data is currently available because the data are currently computationally expensive to produce from the TES radiances. However, updated fluxes can be calculated once the operational code is formally implemented in the Aura TES production computing cluster.

The TES free tropospheric OCS data have been validated against measurements from five HIPPO campaigns and one NOAA oceanic high-altitude site at Mauna Loa (MLO) in [*Kuai et al.*, 2014]. That work shows that the collocated monthly mean TES OCS varies consistently with measurements from five HIPPO campaigns in latitudinal gradient during five different months of the year and consistently with NOAA observations at MLO in the seasonal variation, within a calculated accuracy of about 7 ppt for TES data. For more details, please refer to *Kuai et al.* [2014].

2.2. Forward Model

We use GEOS-Chem, a global chemical transport model, driven by assimilated meteorological data from the NASA Goddard Earth Observing System-5 (GEOS-5) as a forward model for atmospheric composition of OCS.

Table 1. The A Priori OCS Land/Ocean Fluxes Inventory for the GEOS-Chem Simulation of Atmospheric OCS[a]

OCS Global Budget (Gg S yr^{-1})	B2013u
Direct COS flux from oceans	41
Indirect COS flux as CS2 from oceans	83
Indirect COS flux as DMS from oceans	155
Direct anthropogenic flux	62
Indirect anthropogenic flux from CS2	113
Indirect anthropogenic flux from DMS	0
Biomass burning	49 (from GFED3)
Additional ocean flux	559 (evenly distributed)
Destruction by OH radical	−111
Uptake by canopy	−775 (from SiB3)
Uptake by soil	−176 (from SiB3)
Net total	0

[a]B2013u fluxes are similar to *Berry et al.* [2013] except a constant extra source (559 Gg S yr^{-1}) is added to oceanic regions between 40°S and 40°N. The GEOS_Chem simulation was spun up for three years (2004 to 2006).

The OCS concentrations are simulated with a horizontal resolution of 2° × 2.5° and 47 vertical levels driven by GEOS-5 meteorological data and OCS fluxes for the years 2004 to 2006, with a 3 year spin-up. The seasonal variation is quite stable over the 3 year period at the multiple NOAA sites (Figure A1).

The primary land/ocean flux configuration to be used in this work is similar to that reported in *Berry et al.* [2013]. Berry et al.'s inventory included a carbon cycle model, the Simple Biosphere Model (Sib3) [*Baker et al.*, 2007, 2008], of terrestrial fluxes that were ~3 times larger than terrestrial fluxes in Kettle et al.'s inventory (see Introduction). To balance the net uptake, Berry et al. added an ocean source of ~590 Gg S yr^{-1} to the oceanic regions, with a latitudinal distribution that was based on an atmospheric inversion with NOAA air-monitoring data.

Here we simulate OCS using the Berry et al.'s fluxes but with a balanced ocean source that has a uniform latitudinal distribution between 40°N and 40°S. The constant ocean source is defined such that the total extra source term is ~559 Gg S yr^{-1}. We refer to this OCS land/ocean fluxes configuration as the "*Berry et al.* [2013] with uniformly distributed test source inventory" (B2013u; Table 1). For an OCS atmospheric loss term via oxidation by hydroxyl radicals (OH), we used the following destruction equation:

$$\mathrm{OCS} + \mathrm{OH} \rightarrow \mathrm{CO_2} + \mathrm{SH} \left(k = 5.7 \times 10^{-14}\right) \mathrm{cm^3 s^{-1}} \ \text{ at } \ 296 \ \mathrm{K}$$

We implemented the Arrhenius equation applying the OH field from Global Modeling Initiative, the destruction rate with a temperature-dependence, the OH product 2004-2008, and run of HindcastFFIgac2. This simulation is described in *Strode et al.* [2015]. For this reaction, biomolecular rate constant is given in Arrhenius form:

$$k(T) = A \exp\left(-\frac{E}{RT}\right)$$

The A and E/R for the reaction are 1.1E-13 and 1200, respectively [*Sander et al.*, 2011; *Baulch et al.*, 1985].

2.3. Inverse Modeling

Due to the limited information content in the TES free-tropospheric OCS measurements, estimating the land/ocean fluxes at all model grid points is not possible. Instead, the fluxes are estimated over only 24 representative broad regions between 60°N and 60°S (Figure 1). A linear inversion method is used to estimate the state vector of 24 scaling factors, the ratio of the estimated fluxes to the a priori fluxes in each region.

The goal of the inversion method is to optimize the surface fluxes by fitting the simulated monthly mean OCS concentrations in the free troposphere (Y_{mod}) with the TES observations (Y_{obs}). The sensitivity of the atmospheric OCS concentration to the surface flux is defined as a finite difference of the OCS concentrations due to the perturbation of the surface fluxes by 100% from the control run (usually called the Jacobian matrix **K**). By minimizing a cost function (χ^2), the best fitting between modeled and observed values is reached:

$$\chi^2 = \frac{1}{2}\left[(\gamma - \gamma_0)^T \mathbf{S_a}^{-1}(\gamma - \gamma_0) + (Y_{\mathrm{obs}} - Y_{\mathrm{mod}})^T \mathbf{S_e}^{-1}(Y_{\mathrm{obs}} - Y_{\mathrm{mod}})\right] \quad (1)$$

where γ is the state vector to be estimated, the ratio of the estimated fluxes (ϕ) to the a priori fluxes (ϕ_0) [*Rodgers et al.*, 2000].

$$\gamma = \frac{\phi}{\phi_0} = \gamma_0 + \Delta\gamma \quad (2)$$

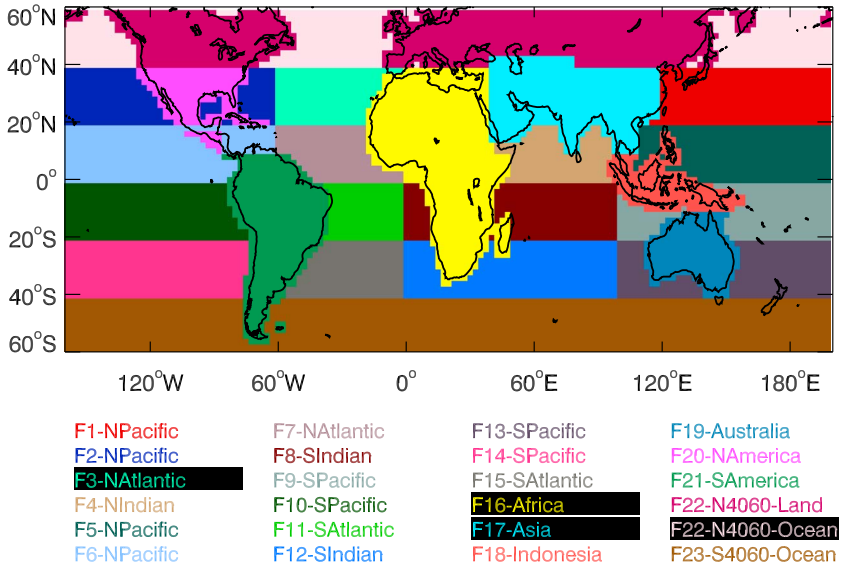

Figure 1. Twenty-four aggregated regions for land/ocean fluxes used in the inversion. F22-N4060-Land will be mentioned as F22-L, and F22-N4060-Ocean will be mentioned as F22-O in the rest of the paper.

where $\gamma_0 = 1$ is the a priori for the state vector. $\mathbf{S_a}$ is the uncertainty covariance matrix for the a priori γ_0 and $\mathbf{S_e}$ is the uncertainty covariance matrix for the TES measurements (Y_o). Minimizing the cost function, the state vector can be estimated as

$$\gamma = \gamma_0 + \mathbf{S_a K}^T \left(\mathbf{K S_e}^{-1} \mathbf{K}^T + \mathbf{S_a}\right)^{-1} \left[\ln(Y_{obs}) - \ln(Y_{mod})\right] \quad (3)$$

More details of the linear inversion are discussed in section A2.

The TES OCS data are averaged onto the GEOS-Chem grid (2° × 2.5°). The standard errors of the grid averages are used to define the diagonal of the measurement covariance matrix. Over most tropical oceanic region, a variance of $(50\%)^2$ is used for the diagonal of the a priori covariance matrix of γ because of the large uncertainties in our current knowledge (Figure 2). The variances at some extratropical oceanic regions and elsewhere, which are less constrained by TES observations, are set to $(10\%)^2$ so that the inverted land/ocean fluxes are more constrained by the a priori information. The covariance matrix is adjusted to ensure that the a posteriori γ cannot be less than -1; i.e., a source or sink must remain as a source or sink after the inversion since the ratio defined between a posteriori flux and a priori flux is $1 + \gamma$.

Different choices for the regularization of the inversion (e.g., increasing the a priori covariance for regions that are not well observed or allowing sources to become sinks or vice versa) do not change our conclusions

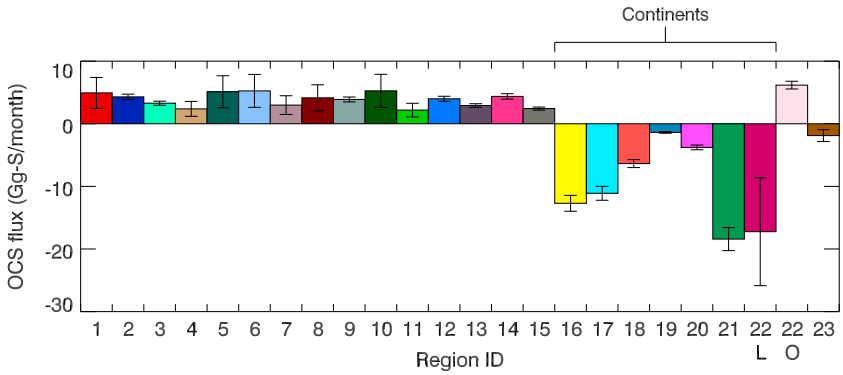

Figure 2. The regional a priori fluxes from the B2013u inventory. Region IDs 16 to 22L are continents; see Figure 1 for details.

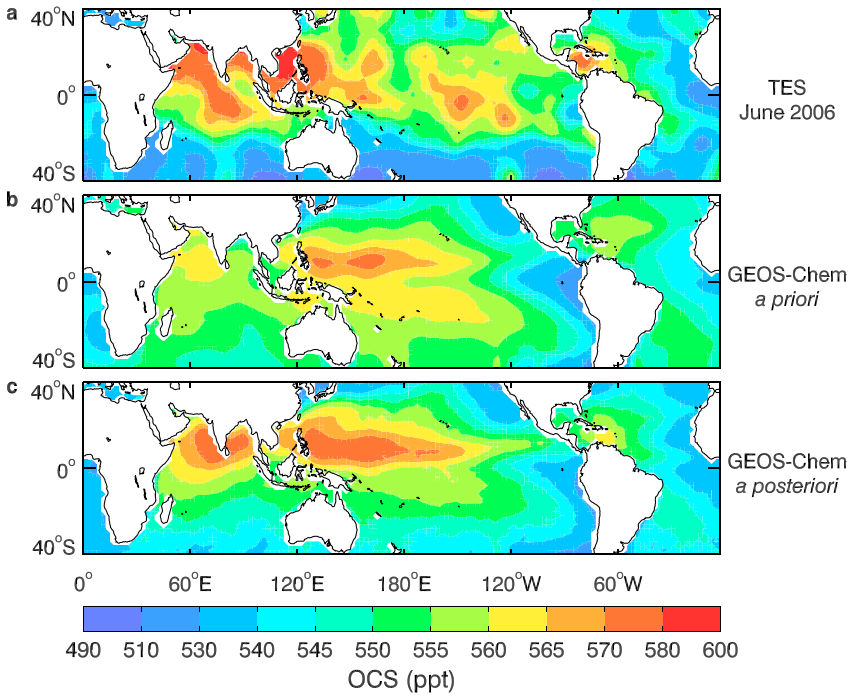

Figure 3. Maps of free troposphere OCS (ppt) for (a) TES measurements in June 2006, (b) a priori GEOS-Chem OCS, and (c) a posteriori OCS. Note that the contour scales are nonlinear.

about tropical ocean fluxes, where the TES data have the most influence, but do nonlinearly affect the regions where the TES data have little sensitivity to OCS fluxes as well as reducing agreement between the a posteriori modeled OCS concentrations and HIPPO measurements. Another important constraint (see section A2) is that we do not allow the total flux to vary; consequently, if a flux in one region goes up (e.g., the Western Pacific) then the flux in another region has to go down.

3. A Case Study for June 2006

Figure 3a shows the monthly averaged OCS mixing ratios observed by TES in June 2006. The observed OCS has higher abundance in the tropics (>570 ppt), especially over the Indo-Pacific region. The observed abundance drops by a few tens of parts per trillion in the subtropics and can be as low as 490 ppt over the Southern Ocean. The GEOS-Chem OCS abundance obtained using the B2013u inventory as the a priori OCS global flux, on the other hand, shows a significantly lower abundance (~565 ppt) in the Indo-Pacific region while it is too high over the Southern Ocean (~545 ppt) (Figure 3b). After the inversion, the a posteriori GEOS-Chem OCS abundance has a larger latitudinal gradient (Figure 3c). The resultant model OCS is ~570 ppt over the Warm Pool over Indonesia and ~530 ppt over the Southern Ocean.

Table 2 lists the ratios between posterior fluxes to a priori fluxes $(\hat{\gamma}_i + 1)$, error reduction after the inversion, and degree freedom of signal (DOFS) for each aggregated region. The DOFS is a quantity that describes how many degrees of freedom for signal are from the measurements [*Rodgers et al.*, 2000]. In this case, the DOFS for each region can range from 0 to 1. Higher DOFS suggests more sensitivity to the actual flux distribution from the observations. The error reduction is defined as the ratio of the uncertainty reduction for $\hat{\gamma}_i$ to the uncertainty of a priori. These two parameters evaluate the quality of the posterior estimates of γ. The regions with error reduction more than 25% and the largest sensitivity, as indicated by the DOFS parameters, are mostly over tropical oceans (highlighted by red cells in Table 2), where the results are more robust. The west Pacific (F1 and F5) and northern Indian Ocean (F4) are where the largest enhancements occur in the posteriori fluxes and with high DOFS (close to 1). The total DOFS is approximately 9 out of 24 for this 24-region flux inversion.

Table 2. A List of Error Reduction and DOFS for Each Aggregated Region[a]

Regions	$\hat{\gamma}+1$	Error reduction	DOFS
F6	2.71	70%	0.91
F5	1.97	69%	0.91
F22-O	4.10	63%	0.87
F10	1.28	57%	0.82
F1	4.11	56%	0.81
F8	2.52	54%	0.79
F7	4.19	52%	0.77
F21	0.38	39%	0.63
F4	5.95	36%	0.59
F11	1.07	29%	0.50
F16	1.28	25%	0.44
F18	0.56	19%	0.35
F17	0.09	15%	0.28
F3	1.10	7%	0.14
F20	0.58	6%	0.12
F9	0.48	6%	0.12
F23	7.91	3%	0.06
F2	0.98	3%	0.06
F12	0.00	1%	0.03
F14	0.17	1%	0.02
F13	0.20	1%	0.02
F19	1.08	1%	0.01
F15	0.47	1%	0.01
F22-L	0.79	0%	0.01

[a]The red cells are tropical ocean regions within ±20° of the equator.

We evaluate the enhanced fluxes over tropical ocean (e.g., west Pacific and northern Indian Ocean) by comparing the resulting posterior OCS distributions from the GEOS-Chem model to those from the HIPPO measurements [*Wofsy et al.*, 2011]. The HIPPO-4 campaign provides in situ aircraft measurements of OCS approximately pole-to-pole across the western-to-central Pacific from mid-June to mid-July in 2011. *Kuai et al.* [2014] have used HIPPO data to validate the latitudinal gradient of the TES OCS abundance. Here the same analysis is applied to the GEOS-Chem OCS simulation. Figure 4 shows the HIPPO-4 flight path, which started northward from the North American Continent to the north of Alaska near 87°N, followed by a southbound route in the central Pacific to the south of Tasmania near 67°S, then went northward to the Warm Pool over the Indonesia, and finally returned to Alaska and the North American Continent. Along the flight path, the aircraft went up and down to different altitudes between the surface and the tropopause. The HIPPO-4 measurements revealed relatively high OCS abundances (>550 ppt) over the west Pacific and relatively low OCS abundances (<530 ppt) over the southern Pacific. The OCS abundances are significantly lower over the continents. To compare with the TES-based a posteriori GEOS-Chem OCS abundance over ocean, HIPPO-4 measurements over the continents (represented by open circles) are ignored because uptake of OCS by land can have a significant effect. Five nonterrestrial NOAA sites coincident

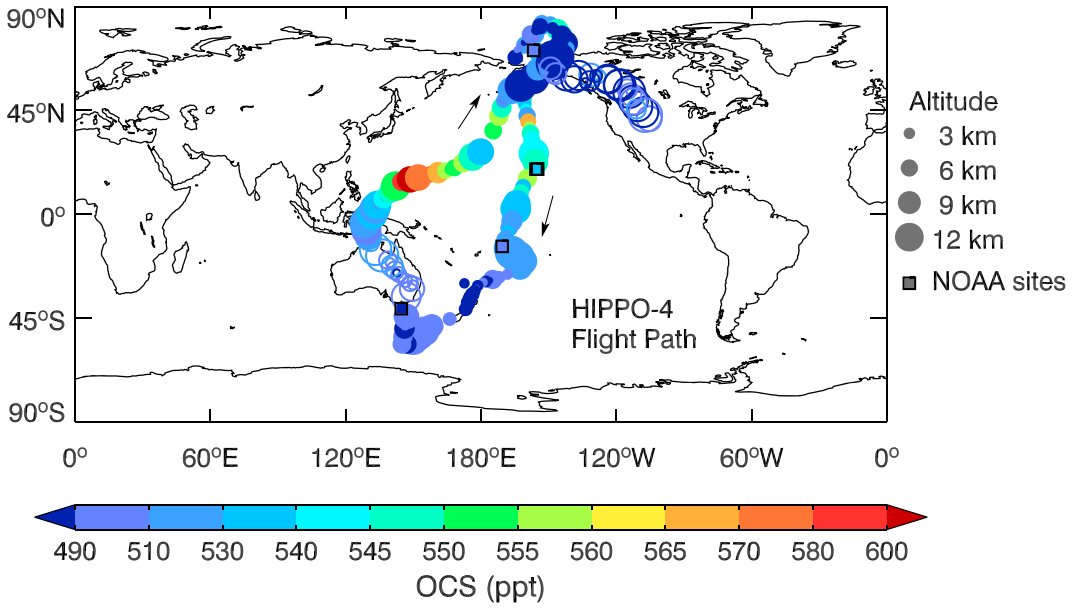

Figure 4. HIPPO-4 measurements of OCS along its flight path between 14 June 2011 and 11 July 2011. For visual purposes, each data point in the graph is an average of seven measurements near the location shown. The solid circles represent HIPPO measurements over oceans that are used for comparisons with the GEOS-Chem outputs. The size of the data point represents the aircraft altitude. Open circles are HIPPO measurements over land. The squares indicate the location of NOAA oceanic sites, and their fill color represents the monthly mean of the surface OCS in June 2011.

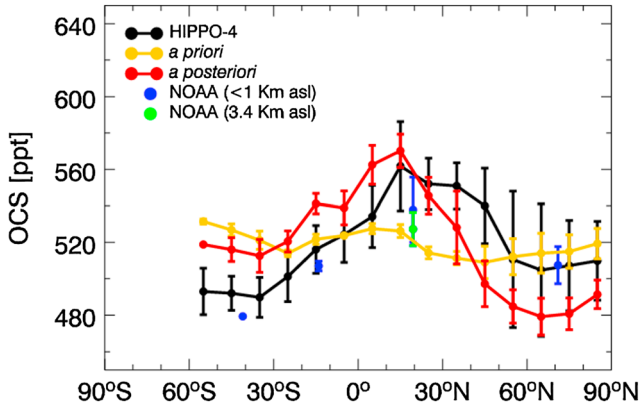

Figure 5. Comparison of the latitudinal variations of the a priori and a posteriori GEOS-Chem OCS abundance with the HIPPO-4 observations. The GEOS-Chem OCS abundances have been vertically shifted such that the means of the a priori and a posteriori are the same as the mean of the HIPPO data (521 ppt). The error bar is calculated as the standard variation of the averaged OCS concentration. Surface measurements at NOAA sites showed previously in Figure 4 are also plotted here. The Mauna Loa site, a high-altitude site, is plotted in green to distinguish it from near-surface observations in blue.

with HIPPO-4 south-bound flight tracks are also plotted to represent the surface OCS observations in Figure 4. Two sites at Hawaii, MLO, and KUM, are overlapped. The small differences between free tropospheric OCS from HIPPO-4 and the surface data from NOAA suggest small vertical gradients over Pacific (e.g., above Hawaii and Rarotonga).

Figure 5 compares the latitudinal dependence of HIPPO-4, a priori, and a posteriori GEOS-Chem OCS abundances. The GEOS-Chem OCS along the HIPPO-4 path (Figure 4) during the month of June are averaged in the same way as the HIPPO data, vertically between 200 and 900 hPa and are binned in a grid every 10°. The HIPPO-4 data show a maximum of ~560 ppt at 15°N and decrease rapidly to the south and more gradually to the

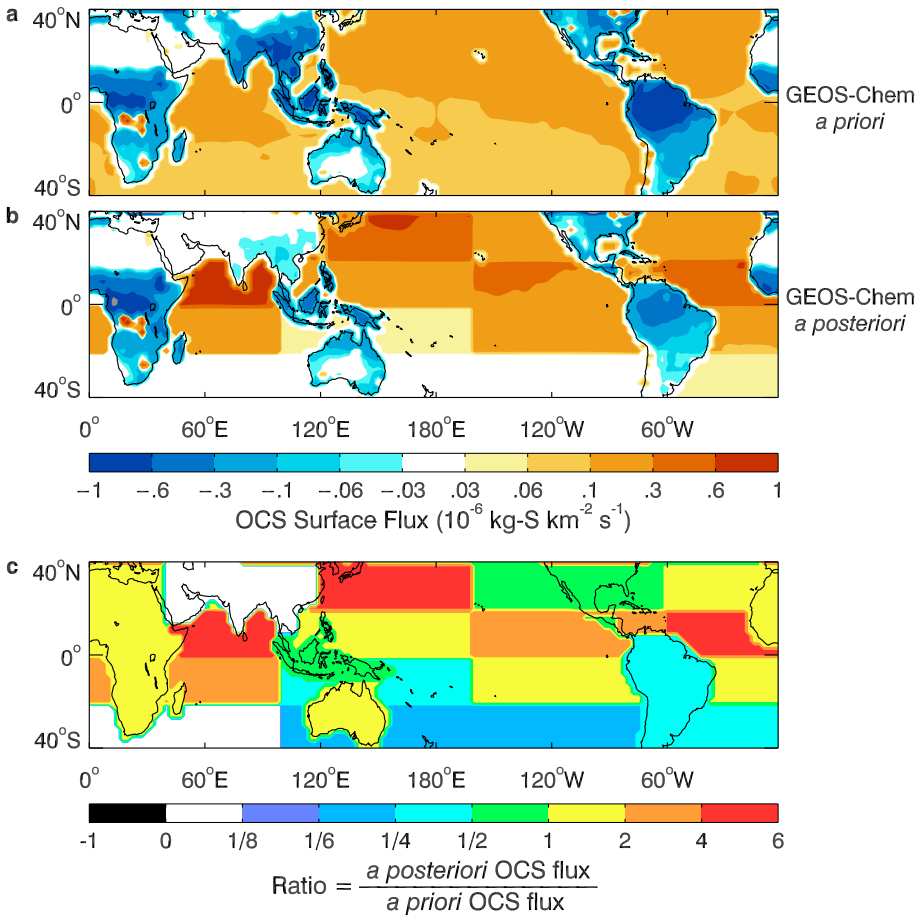

Figure 6. Maps of (a) the B2013u OCS flux inventory and (b) the a posteriori GEOS-Chem inventory. (c) The ratio between the a priori and the a posteriori flux inventory are also shown.

north with a strong latitudinal variation of ~70 ppt between 40°N and 40°S. The a posteriori GEOS-Chem OCS peaks at the same latitude and shows a similar latitudinal variation of ~60 ppt. The magnitude of the posterior latitudinal gradient in GEOS-Chem is greatly improved against the a priori latitudinal gradient; the difference between the peak value in the tropics and the lowest value in the subtropics changes from approximately from 10 ppt (a priori) to approximately 60 ppt (a posteriori) as compared to the HIPPO observed value of approximately 70 ppt. The correlation to HIPPO-4 data is −0.21 for the a priori and is 0.56 for the a posteriori. With a latitudinal phase shift, the correlation for the a priori to HIPPO-4 improves to 0.3 and for a posteriori increases to 0.7. TES data used for inversion are measured in a different year, 2006, compared to the 2011 HIPPO-4 campaign; unfortunately, global summertime data are not available from TES in 2011. The time difference may explain part of the discrepancy between the a posteriori data and HIPPO. The surface data from NOAA (Figure 5) show similar latitudinal variation. HIPPO-4, the a posteriori data constrained by TES, and NOAA data are consistent with each other within the estimated error bars.

Figure 6 compares the a priori B2013u OCS flux inventory (Figure 6a) and the a posteriori GEOS-Chem OCS flux inventory (Figure 6b) at tropical/subtropical latitudes (40°S–40°N). The B2013u inventory is characterized by nearly uniform oceanic sources (~10^{-7} kg S km^{-2} s^{-1}) and a small area of land source (~0.5×10^{-7} kg S km^{-2} s^{-1}) south of Congo from biomass burning. It is also characterized by strong tropical land sinks (–10^{-6} kg S km^{-2} s^{-1}) over the major rainforests, including Congo, Amazon, and southeast Asia; in addition, most of North America is also a significant sink (-0.5×10^{-6} kg S km^{-2} s^{-1}). After the inversion using TES observations, there are notable changes in the a posteriori OCS flux (Figures 6b and 6c): (i) The a posteriori fluxes were enhanced (~2–4 times) over most of the tropical oceans, especially the western Pacific and northern Indian Ocean in the northern hemisphere. (ii) The oceanic source over the southern subtropical oceans between 20°S and 40°S is reduced by at least a few factors (2–6), and it can be an order of magnitude weaker for the ocean south of the African continent. (iii) While the land uptakes over the African, Australian, and Maritime Continents remain approximately the same (changes of less than a factor of 2, represented by the green and yellow regions in Figure 6c), tropical land uptake over the Amazon is significantly reduced by 2–4 times and that over southeast Asia is greatly reduced by an order of magnitude. However, further investigation is needed to confirm these conclusions because these changes could simply be a nonlinear effect of the flux estimation approach; as noted earlier the observed TES OCS concentrations are mostly sensitive to tropical oceanic fluxes and have little sensitivity elsewhere.

Since the season variation is negligible in the tropics, using the TES data constraint, we estimate tropical oceanic flux of 70 ± 16 Gg S month^{-1} in June within ±20° latitudinal zone. When extrapolated over the whole year, the annual total flux is about 840 ± 192 Gg S yr^{-1}, which supports the hypothesis proposed by *Berry et al.* [2013] that the ocean flux is in the higher range of approximately 800 Gg S yr^{-1}.

4. Conclusion

We use a linear inversion algorithm to estimate OCS oceanic fluxes using Aura TES OCS observations for June 2006. These data are used to test the hypothesis proposed by *Berry et al.* [2013] that there is a large ocean flux of approximately 800 Gg S yr^{-1} that is needed to balance the terrestrial sink. The posterior flux estimates derived by the TES data in conjunction with the GEOS-Chem atmospheric transport model support the *Berry et al.* [2013] hypothesis and furthermore suggest that the strongest fluxes originate from the west Pacific and northern Indian Ocean near Southeast Asia.

This work can be extended over the full year once the Aura TES record are available using the Aura TES production algorithm, along with new estimates of soil and anthropogenic fluxes [*Campbell et al.*, 2015; *Maseyk et al.*, 2014].

Appendix A

A1. Comparison of OCS Simulations With NOAA Observations

To test our GEOS-CHEM simulation, we used fluxes of two types of inventory based on *Kettle et al.* [2002] (K2002) and *Berry et al.* [2013] (B2013) (see Table A1). The seasonal variation of simulated

Table A1. Global Sources and Sinks Used for GEOS-CHEM Simulations of Atmospheric OCS[a]

Units: Gg S yr^{-1}	K2002	B2013
Direct COS flux from oceans	41	41
Indirect COS flux as CS2 from oceans	83	83
Indirect COS flux as DMS from oceans	155	155
Direct anthropogenic flux	62	62
Indirect anthropogenic flux from CS2	113	113
Indirect anthropogenic flux from DMS	0	0
Biomass burning	0	49 (GFED3)
Additional ocean flux	0	559
Destruction by OH radical	0	−111
Uptake by canopy (SiB3)	−238	−775 (SiB3)
Uptake by soil	−130	−176 (SiB3)
Net total	86	0
Spin-up	None	2004–2006

[a]K2002 refers to the inventory discussed in *Kettle et al.* [2002] (K2002); B2013 are fluxes similar to those discussed in *Berry et al.* [2013] and are also used as a priori fluxes in our inversion.

surface OCS is compared to selected NOAA sites at middle and high latitude in the northern hemisphere (Figure A1).

The simulated OCS concentrations with lower vegetation uptake (red lines; K2002), in general, have substantially lower seasonal variation compared to NOAA observations, especially over middle-latitude/high-latitude continental sites (e.g., LEF, Wisconsin, United States, and HFM, Harvard Forest, United States) where the seasonal peak-to-peak differences are as high as 150 ppt. The simulation with higher vegetation uptake (blue lines; B2013) has much better agreement with the NOAA data.

A2. A Linear Inversion Model With Constrained Total Fluxes

Let x be the horizontal (longitude and latitude) coordinate, z be the altitude, and $U(x,z)$ be the simulated volume-mixing ratio (vmr) of OCS in some particular month. Note that $U(x,z)$ is implicitly dependent on the seasons as well as the land/ocean fluxes in other months. Let $\phi_b(x)$ be the B2013u flux and

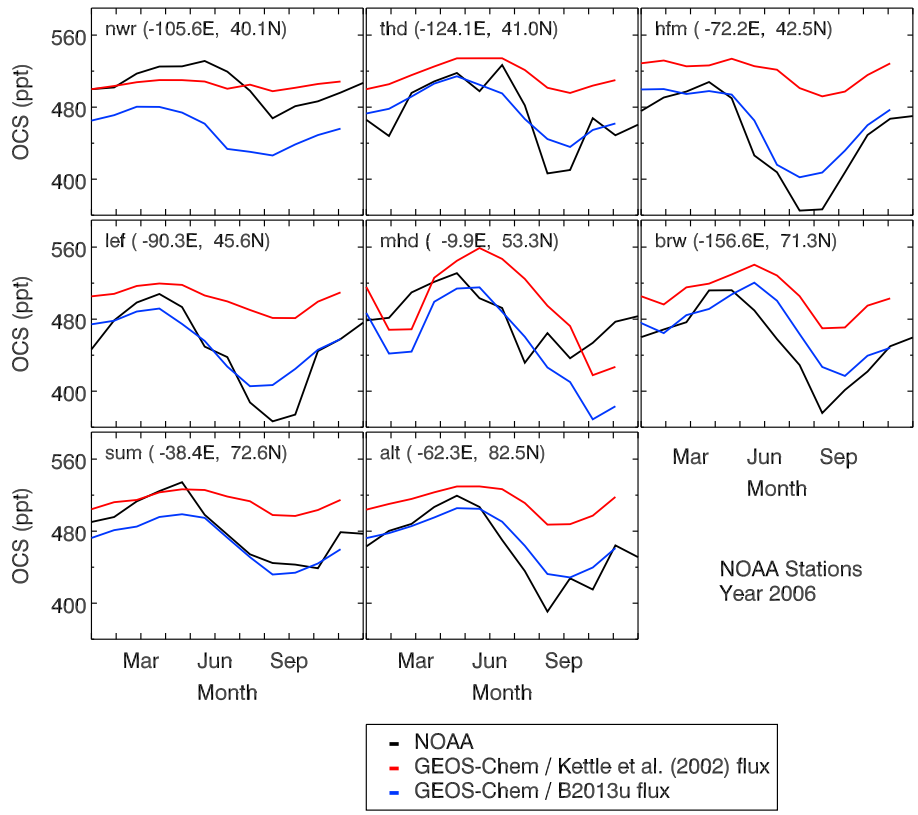

Figure A1. Monthly mean OCS by K2002 (red), B2013 (blue) compared to NOAA observations (black) in 2006.

the resultant vmr be $U_b(x,z)$. If $\phi_b(x)$ over the 24 regions vary by fractions γ_i(i = 1, 2, …, 24), then the resultant vmr can be written as

$$U(x,z) = U_b(x,z) + \sum_{i=1}^{24} \gamma_i K_i(x,z), \tag{A1}$$

where $K_i(x,z)$ is the response function to a fractional change of flux over the ith region x_i. In this work, $K_i(x,z)$ is estimated by the change in $U(x,z)$ when $\phi_b(x)$ is increased by 100% over the ith region.

To compare with TES observations, $U(x,z)$ is convolved to the observational space using the TES vertical averaging kernel $A(z,z')$, assuming that there is no horizontal dependence of A:

$$\ln \widetilde{U}(x,z) = \ln U_a(z) + \int_{z'} A(z,z')[\ln U(x,z') - \ln U_a(z') + \beta]dz', \tag{A2}$$

where $\widetilde{U}$ is the convolved mixing ratio, U_a is the TES a priori OCS concentration (same at all locations), β is a global constant of TES bias correction factor (scalar, not location dependent). Note that the use of the same U_a for all TES retrievals ensures that the variability of retrieved TES OCS was from the TES measured radiances [*Kuai et al.*, 2014]. By accounting for the decrease of the OCS profile in the stratosphere, β is determined to be ~0.2 from the inversion. In practice, the averaging kernel $\mathbf{A}$ is an $n_z \times n_z$ matrix (n_z = number of vertical grid points), $\mathbf{U}$ and $\widetilde{\mathbf{U}}$ are $n_x \times n_z$ matrices (n_x = total number of longitude/latitude grid points), and $\widetilde{\mathbf{U}}_a$ is an n_z-element vector. Then, the integral in equation (2) becomes

$$\ln \widetilde{U}_{jk} = \ln U_{a,k} + \sum_{k'=1}^{n_z} A_{kk'}\left(\ln U_{jk'} - \ln U_{a,k'} + \beta\right), \tag{A3}$$

where $j = 1, 2, \ldots, n_x$ and $k = 1, 2, \ldots n_z$ are the horizontal and vertical indices, respectively. Since the TES OCS data are free tropospheric column averages, $\widetilde{\mathbf{U}}$ is vertically averaged to a column-weighted vmr before comparing with the TES observations:

$$F_j(\gamma,\beta) = \frac{\sum_{k'=1}^{n_z} U_{jk'}\rho_{jk'}\Delta z_{k'}}{\sum_{k'=1}^{n_z} \rho_{jk'}\Delta z_{k'}}, \tag{A4}$$

where F_j is the vertical average of $\widetilde{\mathbf{U}}$ at the jth location, γ is a 24-element vector containing the scaling factors γ_i, ρ_{jk} is a molecular number density at the jth location and the kth vertical layer, and Δz_k is the layer thickness of the kth vertical layer. The dependence on γ and β is explicitly shown in F_j.

In ~~a constrained~~ an unconstrained inversion, the cost function for estimating γ and β is

$$\widetilde{\Psi}(\gamma,\beta) = \frac{1}{2}[\mathbf{Y} - \mathbf{F}(\gamma,\beta)]^T \mathbf{S}_\varepsilon^{-1}[\mathbf{Y} - \mathbf{F}(\gamma,\beta)] + \frac{1}{2}(\gamma - \gamma_a)^T \mathbf{S}_\gamma^{-1}(\gamma - \gamma_a) + \frac{(\beta - \beta_a)^2}{2\sigma_\beta^2}, \tag{A5}$$

where $\mathbf{Y}$ is an n_x-element vector containing the TES OCS data, $\mathbf{F}$ is an n_x-element vector containing F_j, $\mathbf{S}_\varepsilon$ is the measurement covariance matrix, $\boldsymbol{\gamma}_a$ is 24-element vector containing the a priori values of γ, $\mathbf{S}_\gamma$ is the a priori covariance matrix of γ, β_a is the a priori value of β, and σ_β^2 is the a priori variance of β. The Jacobians $\mathbf{J}_\gamma$ (an $n_x \times 24$ matrix) and $\mathbf{J}_\beta$ (an n_x-element vector) with respect to $\boldsymbol{\gamma}$ and β have elements given by

$$\begin{aligned} J_\gamma(x) &= \frac{\partial F}{\partial \gamma_i}(x;\gamma,\beta) = \frac{\sum_{k''=1}^{n_z}\sum_{k'=1}^{n_z} \rho_{jk'} A_{k'k''} K_{ijk''} \widetilde{U}_{jk'} \Delta z_{k'} \Delta z_{k''} / U_{jk''}}{\sum_{k'=1}^{n_z} \rho_{jk'}\Delta z_{k'}}, \\ J_\beta(x) &= \frac{\partial F}{\partial \beta}(x;\gamma,\beta) = \frac{\sum_{k''=1}^{n_z}\sum_{k'=1}^{n_z} \rho_{jk'} A_{k'k''} \widetilde{U}_{jk'} \Delta z_{k'} \Delta z_{k''}}{\sum_{k'=1}^{n_z} \rho_{jk'}\Delta z_{k'}}, \end{aligned} \tag{A6}$$

where $K_{ijk} = K_i(x_j, z_k)$. Since the inversion model is linear, the optimization of the cost function leads to the exact expressions for the estimates of γ and β:

$$\widetilde{\gamma} = \gamma_a + \left(\mathbf{J}_\gamma^T \mathbf{S}_\varepsilon^{-1} \mathbf{J}_\gamma + \mathbf{S}_\gamma^{-1}\right)^{-1} \mathbf{J}_\gamma^T \mathbf{S}_\varepsilon^{-1} \left[\mathbf{Y} - \mathbf{F}(\gamma, \beta) + \mathbf{J}_\gamma^T (\gamma - \gamma_a)\right], \tag{A7}$$

$$\widetilde{\beta} = \beta_a + \left(\mathbf{J}_\beta^T \mathbf{S}_\varepsilon^{-1} \mathbf{J}_\beta + \mathbf{S}_\beta^{-1}\right)^{-1} \mathbf{J}_\beta^T \mathbf{S}_\varepsilon^{-1} \left[\mathbf{Y} - \mathbf{F}(\gamma, \beta) + \mathbf{J}_\beta^T (\beta - \beta_a)\right] \tag{A8}$$

In the inversion process, γ and β on the right-hand sides of equations (A7) and (A8) are the initial guesses (one may use γ_a and β_a as the initial guesses), and $\widetilde{\gamma}$ and $\widetilde{\beta}$ on the left-hand sides are the improved estimates.

In this work, the net total flux will be kept constant during the inversion to maintain a global balanced budget global budget balanced because the atmospheric OCS concentrations are observed with no obvious trend since 2000 [*Montzka et al.*, 2007]. Since the fluxes at high latitude of both hemispheres to be not revised, we constrained the integral of the fluxes over 24 regions are constant, which means if the total source is increased, then the total sink needs to be enhanced as well to balance the changes. This is equivalent to adding a Lagrange multiplier $\lambda \gamma^T \mathbf{\Phi}_b$ to the cost function in equation (A5):

$$\Psi = \widetilde{\Psi} + \lambda \gamma^T \Phi_b \tag{A9}$$

where λ is a multiplier to be determined and $\mathbf{\Phi}_b$ is a 24-element vector with the ith element being the regional total flux over the ith region obtained by area-integrating $\phi_b(x)$ over that region. The resultant β estimator is still given by equation (A8) while a new term proportional to λ is added to equation (A7) for the γ estimator:

$$\hat{\gamma} = \widetilde{\gamma} - \lambda \mathbf{A}^{-1} \Phi_b \tag{A10}$$

$$\hat{\beta} = \widetilde{\beta} \tag{A11}$$

where $\mathbf{A} = \begin{pmatrix} \mathbf{J}_\gamma^T \mathbf{S}_\varepsilon^{-1} \mathbf{J}_\gamma + \mathbf{S}_\gamma^{-1} & \mathbf{J}_\gamma^T \mathbf{S}_\varepsilon^{-1} \mathbf{J}_\beta \\ \mathbf{J}_\gamma^T \mathbf{S}_\varepsilon^{-1} \mathbf{J}_\gamma & \mathbf{J}_\gamma^T \mathbf{S}_\varepsilon^{-1} \mathbf{J}_\beta + \sigma_\beta^{-2} \end{pmatrix}$. As a result, the Lagrange multiplier λ is given by $\widetilde{\gamma} \mathbf{\Phi}_b \left(\mathbf{\Phi}_b^T \mathbf{A}^{-1} \mathbf{\Phi}_b\right)^{-1}$. Equations (A10) and (A11) are used in the OCS flux inversion.

The measurements **Y** to be used is the TES free tropospheric OCS column-averaged data over oceans during the month of June 2006 and is limited to latitudes between 40°N and 40°S. OCS in the GEOS-Chem model, on the other hand, is simulated globally, including over land and ocean. The optimal fluxes $\phi(x)$ over those 24 regions are inverted via the scaling factors γ and bias factor β while the fluxes in other places are fixed.

Acknowledgments

This work was carried out at the Jet Propulsion Laboratory, California Institute of Technology, under a contract with the National Aeronautics and Space Administration. King-Fai Li was supported in part by the UCAR Jack Eddy Fellowship and by the NASA grant (NNX14AR40G) to the University of Washington. Yuk L. Yung acknowledged support by NASA grant (NNX13AK34G) to Caltech. The authors would like to acknowledge Randy Kawa for the help with the OH flux data and also thank Steve Wofsy, Elliot Atlas, Benjamin R. Miller, Fred Moore, James Elkins, and all other HIPPO, NOAA team members (the pilots, mechanics, technicians, and scientific crew) for making the HIPPO and NOAA data available. HIPPO was supported by NSF grants ATM-0628575, ATM-0628519, and ATM-0628388 and by the National Center for Atmospheric Research (NCAR). NCAR is supported by the NSF. The data used in this paper are archived at Jet Propulsion Laboratory and are available from the authors upon request (kl@gps.caltech.edu).

References

Asaf, D., E. Rotenberg, F. Tatarinov, U. Dicken, S. A. Montzka, and D. Yakir (2013), Ecosystem photosynthesis inferred from measurements of carbonyl sulphide flux, *Nat. Geosci.*, *6*(3), 186–190.

Baker, I. T., A. S. Denning, L. Prihodko, K. Schaefer, J. A. Berry, G. J. Collatz, N. S. Suits, R. Stockli, A. Philpott, and O. Leonard (2007), Global Net ecosystem exchange (NEE) of CO2, Oak Ridge Natl. Lab. Distrib. Act. Arch. Cent.

Baker, I. T., L. Prihodko, A. S. Denning, M. Goulden, S. Miller, and H. R. da Rocha (2008), Seasonal drought stress in the Amazon: Reconciling models and observations, *J. Geophys. Res.*, *113*, G00B01, doi:10.1029/2007JG000644.

Baulch, D. L., I. M. Campbell, and S. M. Saunders (1985), Rate constants for the reactions of hydroxyl radicals with propane and ethane, *J. Chem. Soc. Faraday Trans. 1*, *81*, 259–263.

Berry, J., et al. (2013), A coupled model of the global cycles of carbonyl sulfide and CO_2: A possible new window on the carbon cycle, *J. Geophys. Res. Biogeosci.*, *118*, 842–852, doi:10.1002/jgrg.20068.

Campbell, J. E., et al. (2008), Photosynthetic control of atmospheric carbonyl sulfide during the growing season, *Science*, *322*(14), 1085–1088.

Campbell, J. E., M. E. Whelan, U. Seibt, S. J. Smith, J. A. Berry, and T. W. Hilton (2015), Atmospheric carbonyl sulfide sources from anthropogenic activity: Implications for carbon cycle constraints, *Geophys. Res. Lett.*, *42*, 3004–3010, doi:10.1002/2015GL063445.

Charlson, R. J., J. Langner, and H. Rodhe (1990), Sulfate aerosol and climate, *Nature*, *348*(6296), 22–22.

Chin, M., and D. D. Davis (1993), Global sources and sinks of OCS and CS_2 and their distributions, *Global Biogeochem. Cycles*, *7*(2), 321–337, doi:10.1029/93GB00568.

Chin, M., and D. D. Davis (1995), A reanalysis of carbonyl sulfide as a source of stratosphere background sulfer aerosol, *J. Geophys. Res.*, *100*(D5), 8993–9005, doi:10.1029/95JD00275.

Chin, M., and D. J. Jacob (1996), Anthropogenic and natural contributions to tropospheric sulfate: A global model analysis, *J. Geophys. Res.*, *101*(D13), 18,691–18,699, doi:10.1029/96JD01222.

Crutzen, P. J. (1976), Possible importance of CSO for the sulfate layer of stratosphere, *Geophys. Res. Lett.*, *3*(2), 73–76, doi:10.1029/GL003i002p00073.

Kettle, A. J., U. Kuhn, M. von Hobe, J. Kesselmeier, and M. O. Andreae (2002), Global budget of atmospheric carbonyl sulfide: Temporal and spatial variations of the dominant sources and sinks, *J. Geophys. Res.*, *107*(D22), 4658, doi:10.1029/2002JD002187.

Kuai, L., J. Worden, S. S. Kulawik, S. A. Montzka, and J. Liu (2014), Characterization of Aura TES carbonyl sulfide retrievals over ocean, *Atmos. Meas. Tech.*, *7*(1), 163–172.

Launois, T., S. Belviso, L. Bopp, C. G. Fichot, and P. Peylin (2014), A new model for the global biogeochemical cycle of carbonyl sulfide – Part 1: Assessment of direct marine emissions with an oceanic general circulation and biogeochemistry model, *Atmos. Chem. Phys.*, *14*, 20,677–20,720.

Maseyk, K., J. A. Berry, D. Billesbach, J. E. Campbell, M. S. Torn, M. Zahniser, and U. Seibt (2014), Sources and sinks of carbonyl sulfide in an agricultural field in the Southern Great Plains, *Proc. Natl. Acad. Sci. U.S.A.*, *111*(25), 9064–9069.

Montzka, S. A., P. Calvert, B. D. Hall, J. W. Elkins, T. J. Conway, P. P. Tans, and C. Sweeney (2007), On the global distribution, seasonality, and budget of atmospheric carbonyl sulfide (COS) and some similarities to CO_2, *J. Geophys. Res.*, *112*, D09302, doi:10.1029/2006JD007665.

Notholt, J., et al. (2003), Enhanced upper tropical tropospheric COS: Impact on the stratospheric aerosol layer, *Science*, *300*(5617), 307–310.

Notholt, J., H. Bingemer, H. Berresheim, J. R. Holton, A. J. Kettle, E. Mahieu, and S. Montzka (2006), Precursor gas measurement, in *SPARC No.4: Assessment of Stratospheric Aerosol Properties (ASAP)*, edited by L. Thomason and T. Peter, 322 pp., World Clim. Res. Programme, Toronto.

Rodgers, C. D. (2000), *Inverse Methods for Atmospheric Sounding: Theory and Practice*, 256 pp., World Sci., London.

Sander, S. P., et al. (2011), Chemical kinetics and photochemical data for use in atmospheric studies, Evaluation No. 17, JPL Publication 10-6, Jet Propul. Lab., Pasadena, Calif. [Available at http://jpldataeval.jpl.nasa.gov.]

Sandoval-Soto, L., M. Stanimirov, M. von Hobe, V. Schmitt, J. Valdes, A. Wild, and J. Kesselmeier (2005), Global uptake of carbonyl sulfide (COS) by terrestrial vegetation: Estimates corrected by deposition velocities normalized to the uptake of carbon dioxide (CO_2), *Biogeosciences*, *2*(2), 125–132.

Strode, S. A., J. M. Rodriguez, J. A. Logan, O. R. Cooper, J. C. Witte, L. N. Lamsal, M. Damon, B. Van Aartsen, S. D. Steenrod, and S. E. Strahan (2015), Trends and Variability in Surface Ozone over the United States, *J. Geophys. Res. Atmos.*, *120*, doi:10.1002/2014JD022784.

Suntharalingam, P., A. J. Kettle, S. M. Montzka, and D. J. Jacob (2008), Global 3-D model analysis of the seasonal cycle of atmospheric carbonyl sulfide: Implications for terrestrial vegetation uptake, *Geophys. Res. Lett.*, *35*, L19801, doi:10.1029/2008GL034332.

Turco, R. P., R. C. Whitten, O. B. Toon, J. B. Pollack, and P. Hamill (1980), OCS, stratospheric aerosols and climate, *Nature*, *283*, 283–285.

Wofsy, S. C., H. S. Team, M. Cooperating, and T. Satellite (2011), HIAPER Pole-to-Pole Observations (HIPPO): Fine-grained, global-scale measurements of climatically important atmospheric gases and aerosols, *Philos. Trans. R. Soc. A*, *369*(1943), 2073–2086.

Wohlfahrt, G., F. Brilli, L. Hortnagl, X. Xu, H. Bingemer, A. Hansel, and F. Loreto (2012), Carbonyl sulfide (COS) as a tracer for canopy photosynthesis, transpiration and stomatal conductance: Potential and limitations, *Plant Cell Environ.*, *35*(4), 657–667.